

Local quasiparticle lifetimes in a d -wave superconductor

S. Graser,^{1,*} P.J. Hirschfeld,^{1,†} and D.J. Scalapino^{2,‡}

¹*Physics Department, University of Florida, Gainesville, FL 32611 USA*

²*Department of Physics, University of California, Santa Barbara, CA 93106-9530 USA*

(Dated: October 8, 2018)

Scanning tunnelling spectroscopy (STS) measurements find that the surface of Bi-2212 is characterized by nanoscale sized regions, “gap patches,” which have different magnitudes for the d -wave energy gap $\Delta_0(\mathbf{r})$. Recent studies have shown that the tunnelling conductance can be fit using a BCS-type density of states for a d -wave superconductor with a *local* quasiparticle scattering rate. The fit is made with a scattering rate which varies linearly with energy and has a slope $\alpha(\mathbf{r})$ that is positively correlated with the local value of the gap. We consider first the question of what is actually measured in such an experiment. To this end we revisit a model of quasiparticle scattering by impurities and spin fluctuations which was previously used to describe the lifetimes of nodal quasiparticles measured by angle-resolved photoemission (ARPES). We argue that the broadening of the local density of states is determined, except in the case of localized impurity bound states, by the imaginary part of the self-energy of the system averaged over a small region. The size of this region is set by a mean free path which depends upon the energy. At low energies, this region is found to be significantly larger than a gap “patch”, so that the density of states measured by STS is homogeneous in this energy range. At higher energies where the mean free path is comparable with the patch size, the density of states is inhomogeneous. We show that a local self-energy in the impurity-plus-spin fluctuation model, while not strictly linear, yields a local density of states (LDOS) nearly identical to the full theory, and argue that it is consistent with the STS data as well as the phenomenological linear scattering rate extracted from experiment. We also explore the qualitative consequences of this phenomenology for the spectral widths observed in ARPES and predict the existence of Fermi arcs in the superconducting state.

PACS numbers: 74.25.Jb, 74.20.Fg, 74.72.-h

I. INTRODUCTION

For many years, it has been recognized that the properties of the quasiparticle states near the nodes of the d -wave superconducting gap in the cuprates were quite different from those near the gap maxima or antinodes. Transport estimates of nodal mean free paths at low temperatures range from tens of μm in the clean stoichiometric YBCO compounds[1] to hundreds of \AA in dirtier materials like BSCCO[2]. ARPES measurements on BSCCO, with much cruder energy resolution, have reported residual nodal widths of the momentum distribution curve (MDC) of about 10meV[3], which with Fermi velocity values of 10^7 cm/s imply much shorter mean free paths, of order 30 \AA . While this discrepancy is not currently understood, both transport and ARPES *nodal* mean free paths are significantly longer than those extracted from ARPES for *antinodal* quasiparticles. These scattering rates are of order 25-40meV at low T in the optimally doped superconducting state[4], corresponding naively to mean free paths of order a unit cell size. One explanation for this “dichotomy” between nodal and antinodal states that has been proposed is the existence of intense magnetic scattering near the antinodal point

in the underdoped materials due to the proximity of the wave vector \mathbf{Q} connecting the antinodal points by an antiferromagnetic nesting vector. This scattering has also recently been related by several authors to the properties of the “arcs” of coherent Fermi surface in the pseudogap state[5, 6, 7].

Recently, a new perspective has been brought to bear on the properties of these quasiparticle states by STS. In Ref. [8], Alldredge and collaborators succeeded in fitting STS data on Bi-2212 at various dopings to an extremely simple form, that of the local density of states (LDOS) of a d -wave superconductor with a single position and frequency dependent broadening function or scattering rate $\Gamma(\mathbf{r}, \omega)$,

$$N(\mathbf{r}, \omega) = \left\langle \frac{\omega + i\Gamma(\mathbf{r}, \omega)}{(\omega + i\Gamma(\mathbf{r}, \omega))^2 - \Delta_1^2(\mathbf{r})\phi_d(\mathbf{k})^2} \right\rangle. \quad (1)$$

Here

$$\Gamma(\mathbf{r}, \omega) = \Gamma_1(\mathbf{r}) + \Gamma_2(\mathbf{r}, \omega) = \Gamma_1(\mathbf{r}) + \alpha(\mathbf{r})\omega, \quad (2)$$

with $\phi_d(\mathbf{k}) = (\cos k_x - \cos k_y)/2$ and $\alpha(\mathbf{r})$ a constant of proportionality which was found to vary from point to point over the sample surface, and to be strongly and positively correlated with the size of the local gap parameter $\Delta_1(\mathbf{r})$. The frequency independent term Γ_1 simulates the effect of near unitarity limit in-plane scatterers, which are observed as “native defect” resonances in conductance maps of the Bi-2212 surface. Values of Γ extracted from

*Electronic address: graser@phys.ufl.edu

†Electronic address: pjh@phys.ufl.edu

‡Electronic address: djs@physics.ucsb.edu

this fit procedure tended to be much smaller than quasiparticle widths determined by ARPES, ranging at energy $\omega = \langle \Delta_1 \rangle$ from about 2 meV for an optimally doped sample to about 20 meV for a strongly underdoped sample. These results, and the apparent contradiction with ARPES, lead us to consider the following questions:

- What sort of scattering rate is actually being measured in the STS measurement?
- When is it possible to think of a local probe measuring a scattering rate averaged over a region or over disorder, and what length scales define such a region?
- How can the spatially modulated Γ_2 at *low* energies implied by Eq. (2) be reconciled with the observed *homogeneity* of the low-energy quasiparticle states seen in STS?
- Are the results of Ref. [8] possibly consistent with scattering rates other than pure linear in ω , derivable from microscopic models?
- How are the small values of the STS-determined scattering rates to be reconciled with ARPES?

In the following we attempt to answer these questions within a phenomenological framework which assumes as its starting point that there are nanoscale energy gap inhomogeneities. Various suggestions regarding the origin of this “gap patch” inhomogeneity have been proposed[9, 10, 11, 12, 13, 14, 15]. Here we will simply assume that for $T \ll T_c$, the superconducting gap has such nanoscale patch inhomogeneities. We will then proceed in several stages. In Section II we discuss the local density of states of a disordered system, and the conditions under which a system may be considered to be locally self-averaging. We then extend these considerations to inelastic scattering, and discuss what may be deduced from the qualitative aspects of the STS results. In Section III we introduce a model for scattering from impurities, including native defects in the CuO_2 planes, and dopant disorder away from the planes. To the disorder-averaged impurity self-energy we then add the self-energy due to scattering from spin fluctuations, and discuss the anisotropy of the total scattering in momentum space. We then calculate the LDOS from the local Green’s function in Section IV, and compare the results with those computed from a model “local self-energy”. We show that the spectrum may equally well be fit by an assumed linear scattering rate, as proposed in Ref. [8]. Finally, we discuss the extension of the results obtained for the homogeneous *d*-wave superconductor to the inhomogeneous case. We discuss how the spatially homogenous low-energy conductance seen in the STS experiments for $\omega \lesssim \Delta_0$ and the heterogeneous behavior for $\omega \gtrsim \Delta_0$ may be understood within this framework. In addition, we point out the implications of Ref. [8] for the interpretation of ARPES spectra in the superconducting state.

II. GENERAL CONSIDERATIONS

We begin by assuming that STS probes the LDOS, i.e. the imaginary part of the local Green’s function $G(\mathbf{r}, \mathbf{r})$; that is, we assume that the tunnelling matrix elements are constant. For the moment we focus on disorder in the normal metallic state, and neglect interactions. In this case one should in principle calculate G for a given configuration of impurities. There is no notion of a spatially or disorder averaged self-energy which need appear, if one can calculate $G(\mathbf{r}, \mathbf{r})$ for a system with disorder. Indeed, the exact local Green’s function may be written

$$G(\mathbf{r}, \mathbf{r}; \omega) = \sum_n \frac{|\psi_n(\mathbf{r})|^2}{\omega - E_n + i0^+}, \quad (3)$$

where $\psi_n(\mathbf{r})$ are the exact eigenfunctions of the many-electron system in the presence of a given random disorder configuration. Such a calculation would include all interference processes from these many impurities.

Note that even if we are interested exclusively in the local Green’s function, it is far from obvious that one may speak of a local self-energy or scattering rate, as proposed by the STS experiments. This is because the self-energy is formally a nonlocal quantity as is seen from the Dyson equation for $G(\mathbf{r}, \mathbf{r})$:

$$G(\mathbf{r}, \mathbf{r}) = G_0(0) + G_0(\mathbf{r} - \mathbf{r}')\Sigma(\mathbf{r}', \mathbf{r}'')G(\mathbf{r}'', \mathbf{r}), \quad (4)$$

where G_0 is the Green’s function of the homogeneous system. Σ may be treated as local, $\Sigma(\mathbf{r}, \mathbf{r}') \sim \Sigma(\mathbf{r})\delta(\mathbf{r} - \mathbf{r}')$ only if $\Sigma(\mathbf{r}, \mathbf{r}')$ decays sufficiently rapidly.

Under some circumstances it is appropriate to approximate the many-impurity Green’s function by a homogeneous disorder-averaged Green’s function \bar{G} . In a dirty metal, the wave functions $\psi(\mathbf{r})$ decay on a length scale of the mean free path ℓ of the system, as do the disorder averaged Green’s functions and self-energies. This will then be a good description of the system *provided* there are no bound state wave functions present where electrons are confined to within a radius ℓ_b substantially smaller than ℓ . Near the bound state energy $\bar{G}(\mathbf{r}, \mathbf{r}; \omega)$ will provide a poor description of the spatial and spectral properties of this state.

Similar considerations apply to quasiparticles in superconductors. In general, a local measurement by STS will probe wavefunctions spread out over a mean free path. However, one should be wary in a highly anisotropic system like a *d*-wave superconductor of assuming the relevance of mean free paths extracted from other measurements. For example, transport measurements at low T yield the mean free paths of nodal quasiparticles only, and can be very long, whereas an STS experiment probing the system locally at bias ω will involve quasiparticles with a momentum spread ω/v_F and these may well have shorter mean free paths. We will see that results of the STS measurements may be used to determine the typical mean free path of the excitation being measured. In general, however, the system may indeed be taken to be

self-averaging and a treatment in terms of a disorder-averaged \bar{G} should be adequate.

An exception occurs again in the case of impurity bound states, known to occur in the cuprate materials for Cu substituents in the CuO_2 plane. As observed by STM, in these cases a very narrow spectral resonance is found at frequency Ω_0 on the impurity site and near neighbors. The naive calculation of the size of these states at resonance yields

$$\ell_b = \frac{\xi_0}{\sqrt{1 - \frac{\Omega_0^2}{\Delta_0^2}}}, \quad (5)$$

where Δ_0 is the gap maximum and $\xi_0 = v_F/(\pi\Delta_0)$, except in the nodal directions, where $\psi_b \sim 1/r$ and ξ_0 diverges. Note that the electron unbinds when the resonance moves into the continuum $\Omega_0 > \Delta_0$, corresponding to weak impurity potential. More detailed analysis shows that the length scale ℓ_b given above represents the asymptotic long-range decay of the wavefunctions in non-nodal directions; most of the decay away from the impurity site actually takes place over an atomic distance. In any case, for in-plane impurities, $\ell_b \ll l$, so they should be (and are) imaged individually by STS. On the other hand, the out-of-plane dopant atoms in the BSCCO-2212 material have weak potentials and no resonance, corresponding to an essentially infinite ℓ_b , i.e. a disorder averaged calculation of the local Green's function is again appropriate. We conclude that a disorder-averaged \bar{G} is a good representation of the local exact $G(\mathbf{r}, \mathbf{r})$ over a length scale of size ℓ except within a distance ℓ_b of strong impurities. Therefore the notion of a local self-energy or scattering rate will also have meaning, except for a small set of exceptional points.

III. MODEL FOR SCATTERING

The purpose of this section is to present the results of a scattering-rate analysis of spin fluctuations and impurities which will be used to determine the local \bar{G} . We assume that a self-averaged description is appropriate, and investigate, in the BSCCO system, what the sources of scattering are, and how they enter the local \bar{G} . We can then ask if a description in terms of a local self-energy or scattering rate is sensible or not, and whether or not a fit to the LDOS obtained from \bar{G} can also be obtained with a linear scattering rate as proposed in Ref. [8]. This will give us information as to the robustness of such a fit.

A. Elastic potential scattering

The elastic scattering in BSCCO can arise from impurities and disorder inside the conducting copper oxide planes (in-plane impurities) or due to impurities in the neighboring metal oxide planes (out-of-plane impurities). While the in-plane impurities are well characterized

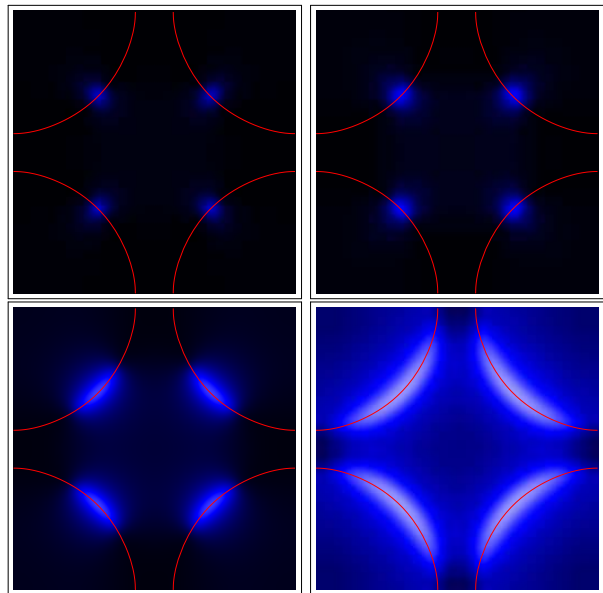


FIG. 1: (Color online) The first two terms of Eq. (15) (τ_0 and the τ_1 contributions) to the elastic scattering rate as a function of k_x and k_y in the first Brillouin zone for different quasiparticle energies ω . From left to right and top to bottom ω is chosen to be $\omega = 0.1\Delta_0$, $\omega = 0.2\Delta_0$, $\omega = 0.5\Delta_0$ and $\omega = \Delta_0$. The red line shows the Fermi surface obtained from the single $t - t'$ band described in the text. The inverse range of the impurity potential is $\kappa = 0.2$, corresponding to strong forward scattering. The color scale is the same for all four plots.

by a point-like isotropic scattering potential, the out-of-plane impurities are better described by a long range e.g. Yukawa type impurity potential leading to a more or less pronounced forward scattering [16, 17, 19]. Since the out-of-plane impurity scattering is relatively weak it can be treated within the self-consistent Born approximation. The elastic self-energy is then given by

$$\underline{\Sigma}_{\text{el}}(\mathbf{k}, \omega) = n_i \sum_{\mathbf{k}'} |V(\mathbf{k}, \mathbf{k}')|^2 \tau_3 \underline{G}(\mathbf{k}', \omega) \tau_3 \quad (6)$$

where τ_α are the Pauli matrices in particle hole space, n_i is the impurity concentration and $V(\mathbf{k}, \mathbf{k}')$ characterizes the momentum dependent impurity potential. Within our calculations we will model it by a screened exponential falloff of the form

$$|V(\mathbf{k}, \mathbf{k}')|^2 = \frac{|V_0|^2}{|\mathbf{k} - \mathbf{k}'|^2 + \kappa^2} \quad (7)$$

where κ^{-1} characterizes the range of the impurity potential. For $\kappa \rightarrow \infty$ the case of isotropic scattering is recovered. The full Green's function $G(\mathbf{k}, \omega)$ can be calculated from the Dyson equation

$$\underline{G}^{-1}(\mathbf{k}, \omega) = \underline{G}_0^{-1}(\mathbf{k}, \omega) - \underline{\Sigma}_{\text{el}}(\mathbf{k}, \omega) \quad (8)$$

where $G_0(\mathbf{k}, \omega)$ describes the pure superconducting state without scattering. Decomposing the self energy into its

different Nambu components leads us to the following three equations which must be solved self-consistently

$$\Sigma_{el,0}(\mathbf{k}, \omega) = n_i \sum_{\mathbf{k}'} |V(\mathbf{k}, \mathbf{k}')|^2 \frac{\tilde{\omega}}{\tilde{\omega}^2 - \tilde{\epsilon}_{\mathbf{k}'}^2 - \tilde{\Delta}_{\mathbf{k}'}}^2}, \quad (9)$$

$$\Sigma_{el,1}(\mathbf{k}, \omega) = -n_i \sum_{\mathbf{k}'} |V(\mathbf{k}, \mathbf{k}')|^2 \frac{\tilde{\Delta}_{\mathbf{k}'}}{\tilde{\omega}^2 - \tilde{\epsilon}_{\mathbf{k}'}^2 - \tilde{\Delta}_{\mathbf{k}'}}^2} \quad (10)$$

and

$$\Sigma_{el,3}(\mathbf{k}, \omega) = n_i \sum_{\mathbf{k}'} |V(\mathbf{k}, \mathbf{k}')|^2 \frac{\tilde{\epsilon}_{\mathbf{k}'}}{\tilde{\omega}^2 - \tilde{\epsilon}_{\mathbf{k}'}^2 - \tilde{\Delta}_{\mathbf{k}'}}^2} \quad (11)$$

Here $\tilde{\omega} = \omega - \Sigma_{el,0}(\mathbf{k}, \omega)$, $\tilde{\epsilon}_{\mathbf{k}} = \epsilon_{\mathbf{k}} + \Sigma_{el,3}(\mathbf{k}, \omega)$ and $\tilde{\Delta}_{\mathbf{k}} = \Delta_{\mathbf{k}} + \Sigma_{el,1}(\mathbf{k}, \omega)$ are the renormalized quasiparticle energy, band structure and pairing potential respectively. For our numerical calculations, we will use a simple tight-binding parameterization of the band structure including nearest and next nearest neighbor hopping

$$\epsilon_{\mathbf{k}} = -2t (\cos k_x + \cos k_y) - 4t' \cos k_x \cos k_y - \mu \quad (12)$$

with a d -wave order parameter

$$\Delta_{\mathbf{k}} = \frac{\Delta_0}{2} (\cos k_x - \cos k_y). \quad (13)$$

To model the Fermi surface in the cuprates we use $t' = -0.35t$ and $\mu = -1.1t$, with energy measured in units of nearest neighbor hopping t . The temperature dependence of the gap is parameterized by the simple form

$$\Delta_0(T) = \Delta_0 \tanh \left(\alpha \sqrt{\frac{T_c}{T} - 1} \right) \quad (14)$$

with $\alpha = 3$, $2\Delta_0/kT_c = 6$, and $\Delta_0 = 0.2t$.

The elastic scattering rate, broadening the quasiparticle state with energy ω , is determined by the denominator of the full Green's function and can be calculated approximately from the pole of G as

$$\Gamma_{el}(\mathbf{k}, \omega) = -\text{Im} \left(\Sigma_{el,0}(\mathbf{k}, \omega) + \frac{\Delta_{\mathbf{k}}}{\omega} \Sigma_{el,1}(\mathbf{k}, \omega) + \frac{\epsilon_{\mathbf{k}}}{\omega} \Sigma_{el,3}(\mathbf{k}, \omega) \right) \quad (15)$$

For quasiparticles at the Fermi surface only the imaginary parts of $\Sigma_{el,0}$ and $\Sigma_{el,1}$ contribute to the elastic scattering rate. To compare our results for different impurity ranges, we have normalized the scattering rates in a way that the (normal conducting) scattering rate for T_c taken at the nodal point of the Fermi surface \mathbf{k}_N equals $0.1\Delta_0$. All calculations for the elastic as well as for the inelastic scattering rate have been performed for a low temperature $T = 0.1T_c$ unless otherwise stated.

In Fig. 1 we show the imaginary part of the τ_0 and the τ_1 contribution of the elastic self energy to $\Gamma_{01} \equiv$

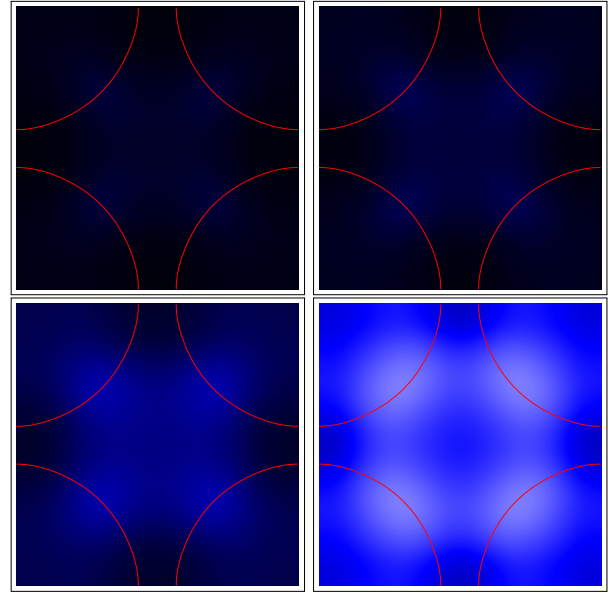


FIG. 2: (Color online) Same as Fig. 1, but with less pronounced forward scattering, $\kappa = 1.0$.

$-\text{Im} \Sigma_{el,0} - \Delta_{\mathbf{k}}/\omega \text{Im} \Sigma_{el,1}$, that describes the elastic quasiparticle scattering rate (we have neglected the $\Sigma_{el,3}$ term in (15), which vanishes on the Fermi surface, in order to highlight the behavior there). In the case of a distinct forward scattering potential with $\kappa = 0.2$, it is obvious that nodal quasiparticles can be scattered at low energies while the scattering of antinodal quasiparticles is strongly suppressed. In Fig. 2, we show the same quantity for a more isotropic scattering potential with $\kappa = 1$. Here the elastic scattering rate for quasiparticles at the Fermi surface shows only a weak anisotropy with just a slightly increased scattering rate for nodal quasiparticles. With increasing κ , approaching the isotropic limit, the elastic scattering rate at the Fermi surface is fully determined by the imaginary part of $\Sigma_{el,0}$ while $\Sigma_{el,1}$ vanishes.

In Fig. 3, we compare the energy dependence of the nodal and antinodal elastic scattering rates for the two different forward scattering parameters discussed above. We find for the elastic scattering in the forward scattering limit ($\kappa = 0.2$) a high scattering rate for nodal quasiparticles already at low energies compared to the gap Δ_0 , while the scattering rate for quasiparticles at the antinodal points is strongly suppressed and sets in only for higher energies [17]. As previously discussed [18], this behavior arises from a cancellation between the “normal” Σ_0 and the “anomalous” Σ_1 channels for $\omega < \Delta_{\mathbf{k}}$ when the scattering is peaked in the forward direction. As expected, the scattering becomes more isotropic if the range of the impurity potential is decreased ($\kappa = 1$) and the frequency dependent scattering rates evaluated at different points of the Fermi surface approach each other. In this case, the scattering rate for nodal quasiparticles as

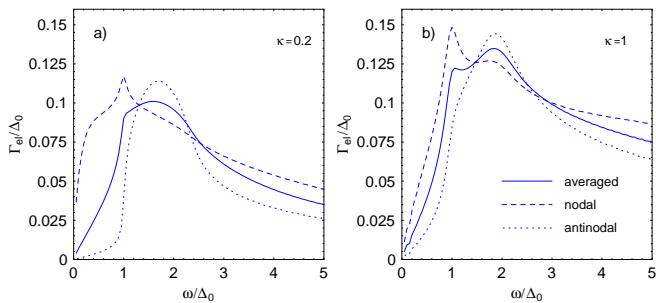


FIG. 3: (Color online) The elastic scattering rate as a function of the quasiparticle energy ω for two different values of the inverse scattering range $\kappa = 0.2$ (a) and $\kappa = 1$ (b). The solid lines show the scattering rate averaged over the Fermi surface, while the dashed and dotted lines show the scattering rate for quasiparticles at the nodal and antinodal point of the Fermi surface respectively.

well as the Fermi surface averaged scattering rate shows a nearly linear increase with frequency, reflecting the d -wave density of states.

B. Elastic off-diagonal scattering

We mention briefly the notion of off-diagonal or pairing disorder scattering by out of plane impurities, claimed to be responsible in Refs. [12, 13, 14, 20, 21, 22] for the inhomogeneity in the gap magnitude measured by STS, as well as for many of the correlations between various STS observables. The scenario described in these works is that out of plane dopant impurities, in addition to creating a screened Coulomb potential, represent an atomic-scale modulation of the BCS pairing interaction in the low-energy effective Hamiltonian, via a modulation of local electronic structure parameters such as t, t' or J , or of electron-phonon interaction matrix elements. Since the scattering by an induced off-diagonal potential $\delta\Delta(\mathbf{r})$ is necessarily weak on the scale of the Fermi energy, it is again appropriate to use the Born approximation to describe this scattering. The modulation of $\Delta(\mathbf{r})$ observed in experiment [23, 24, 25] is however not pointlike, but has a characteristic wavelength of 25-30 Å; within the picture of Ref. [12], this arises because the dopant atoms give rise to an atomic scale modulation of the BCS pairing potential which causes larger, coherence

length size fluctuations in $\Delta_{\mathbf{k}}(\mathbf{r})$. This is somewhat difficult to model as a quasiparticle scattering potential in a disorder averaged calculation (see however [26]), so we try in Appendix 1 to estimate the crude effect of order parameter modulations on quasiparticle scattering by allowing the order parameter to be modulated on the 4 bonds around the impurity, while assuming that it retains its d -wave character[27]. We find, not surprisingly, that the scattering rate is largest at the antinode, where it rises linearly in ω at zero temperature.

In an inhomogeneous system like BSCCO-2212, one might take $\delta\Delta_{\mathbf{k}}$ to be of order Δ_0 to reflect the large distribution of observed gap values in the system. The overall scale of the scattering parameter Γ^{Δ} defined in the Appendix would then vary as Δ_0^2 , leading to an averaged local scattering rate of $\sim \Delta_0\omega$. It is tempting to speculate that the measured strong correlation of the STS scattering rate coefficient $\alpha(\mathbf{r})$ defined in (1)-(2) with the local $\Delta(\mathbf{r})$ is due to this effect, but a much more rigorous treatment is needed to establish this.

The results in Appendix 1 give a rough measure of the additional scattering rate due to the τ_1 or pairing disorder component. This would apply, however, only in situations where the quasiparticles explore many gap “patches”, such that a pairing disorder scenario is valid. However, as we argue below, this is the case only at low energies, where the STS presents a picture of homogeneous electronic structure. At higher energies, such averaging is no longer appropriate, and it would be interesting to consider in more detail the effects of localization of quasiparticles within a patch, see Refs. [12] and [14]. Since a more microscopic approach is not available at the present time, *and* a momentum average will clearly give an overall linear- ω contribution to the elastic scattering rate arising from this term (similar to the ordinary Coulomb scattering), we will ignore its possible relevance for the time being and return to it only in the discussion.

C. Inelastic electron-electron scattering

Besides the elastic scattering we will also take into account the inelastic scattering that arises from the exchange of dynamic spin fluctuations. In the random-phase approximation (RPA), the imaginary part of the quasiparticle self-energy due to inelastic scattering from the on-site Coulomb interaction U can be written as [28]

$$\begin{aligned}
 -\text{Im } \Sigma_{\text{inel}}(\omega, \mathbf{k}) &= \frac{3U^2}{4} \sum_q [n(\omega - E_{\mathbf{q}}) + f(-E_{\mathbf{q}})] \text{Im } \chi(\mathbf{k} - \mathbf{q}, \omega - E_{\mathbf{q}}) \left(\tau_0 + \frac{\epsilon_{\mathbf{q}}}{E_{\mathbf{q}}} \tau_3 + \frac{\Delta_{\mathbf{q}}}{E_{\mathbf{q}}} \tau_1 \right) \\
 &+ \frac{3U^2}{4} \sum_q [n(\omega + E_{\mathbf{q}}) + f(E_{\mathbf{q}})] \text{Im } \chi(\mathbf{k} - \mathbf{q}, \omega + E_{\mathbf{q}}) \left(\tau_0 - \frac{\epsilon_{\mathbf{q}}}{E_{\mathbf{q}}} \tau_3 - \frac{\Delta_{\mathbf{q}}}{E_{\mathbf{q}}} \tau_1 \right)
 \end{aligned} \quad (16)$$

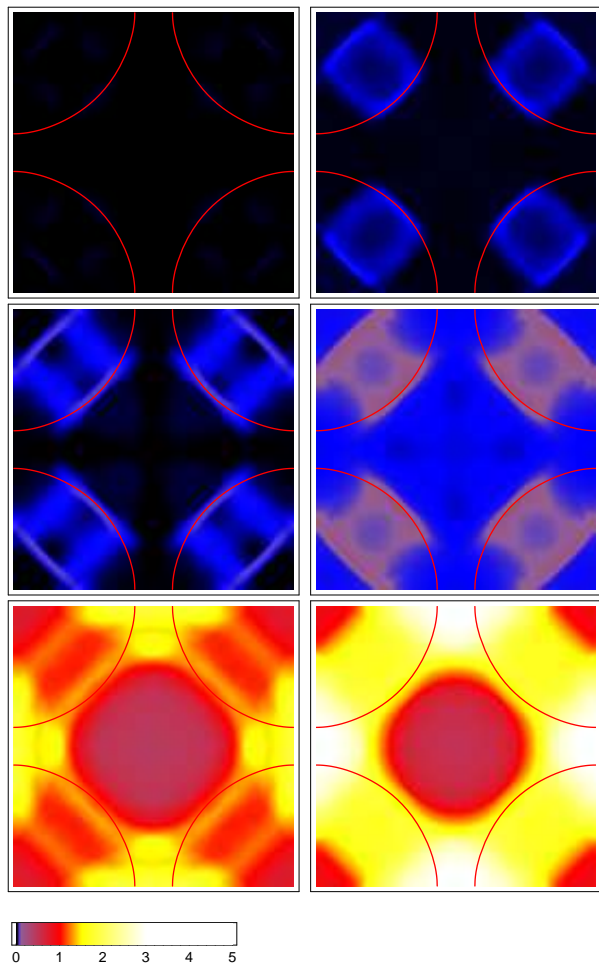


FIG. 4: (Color online) The sum of the τ_0 and the τ_1 contributions to the inelastic scattering rate (which determine the scattering near the Fermi surface) as a function of k_x and k_y in the first Brillouin zone for different quasiparticle energies ω . In the left column the coupling constant is taken to be $\bar{U} = 2.20t$, which does not produce a well-defined resonant mode. In the right column we show results for $\bar{U} = 2.36t$, which produces a resonant mode and an incommensurate spin response. From top to bottom ω is chosen to be $\omega = 0.5\Delta_0$, $\omega = \Delta_0$ and $\omega = 2.5\Delta_0$. The red line shows the Fermi surface. The color scale is the same for all six plots and is given below. The units of the scattering rate Γ shown in the color bar are Δ_0 .

In this expression $n(\omega)$ and $f(\omega)$ are the Bose and Fermi distribution functions, $E_{\mathbf{k}} = \sqrt{\epsilon_{\mathbf{k}}^2 + \Delta_{\mathbf{k}}^2}$ and the RPA expression for the spin susceptibility χ is given by

$$\chi(\mathbf{k}, \omega) = \frac{\chi_0(\mathbf{k}, \omega)}{1 - \bar{U}\chi_0(\mathbf{k}, \omega)}, \quad (17)$$

where χ_0 is the bare BCS spin susceptibility

$$\begin{aligned} \chi_0(\mathbf{q}, \omega) = & \sum_{\mathbf{k}} \left\{ \frac{1}{2} \left[1 + \frac{\epsilon_{\mathbf{k}+\mathbf{q}}\epsilon_{\mathbf{k}} + \Delta_{\mathbf{k}+\mathbf{q}}\Delta_{\mathbf{k}}}{E_{\mathbf{k}+\mathbf{q}}E_{\mathbf{k}}} \right] \frac{f(E_{\mathbf{k}+\mathbf{q}}) - f(E_{\mathbf{k}})}{\omega - (E_{\mathbf{k}+\mathbf{q}} - E_{\mathbf{k}}) + i0^+} \right. \\ & + \frac{1}{4} \left[1 - \frac{\epsilon_{\mathbf{k}+\mathbf{q}}\epsilon_{\mathbf{k}} + \Delta_{\mathbf{k}+\mathbf{q}}\Delta_{\mathbf{k}}}{E_{\mathbf{k}+\mathbf{q}}E_{\mathbf{k}}} \right] \frac{1 - f(E_{\mathbf{k}+\mathbf{q}}) - f(E_{\mathbf{k}})}{\omega + (E_{\mathbf{k}+\mathbf{q}} + E_{\mathbf{k}}) + i0^+} \\ & \left. + \frac{1}{4} \left[1 - \frac{\epsilon_{\mathbf{k}+\mathbf{q}}\epsilon_{\mathbf{k}} + \Delta_{\mathbf{k}+\mathbf{q}}\Delta_{\mathbf{k}}}{E_{\mathbf{k}+\mathbf{q}}E_{\mathbf{k}}} \right] \frac{f(E_{\mathbf{k}+\mathbf{q}}) + f(E_{\mathbf{k}}) - 1}{\omega - (E_{\mathbf{k}+\mathbf{q}} + E_{\mathbf{k}}) + i0^+} \right\}. \end{aligned}$$

Note that in (16) the coupling constant U is in principle different from the effective \bar{U} that enters the denominator of the RPA expression Eq. (17) for the spin susceptibility. Here U and \tilde{U} will be treated as phenomenological parameters. Earlier numerical calculations have used $U = \bar{U} = 2.2t$, to fit microwave and thermal conductivity [29, 32]. Here we will set $U = 2.2t$ and vary \bar{U} in order to see what effects a π -resonance produces.

In Fig. 4 the sum of the imaginary parts of the τ_0 and τ_1 component of the inelastic scattering rate, which determines the inelastic scattering of quasiparticles at the Fermi surface, are shown in momentum space for the choice $U = \bar{U} = 2.2t$ (left column) and $\bar{U} = 2.36t$ (right column). Besides the strong scattering peaks at the Fermi surface, we find equally strong signals near the corner of the Brillouin zone, that are visible for all energies ω and reflect the enhanced spin susceptibility at the nesting vectors connecting the two opposite branches of the Fermi surface.

The energy dependence of the scattering rate at the nodal and antinodal points on the Fermi surface for $\bar{U} = 2.2t$ is now exhibited in Fig. 5(a) and (b). In contrast to the elastic rate, the inelastic scattering rate at $T = 0$ is strongly suppressed for low energies and shows an ω^3 dependence for nodal quasiparticles [28, 29, 30, 31, 32] while it vanishes exponentially below Δ_0 for antinodal quasiparticles. (Note that in the reference clean noninteracting quasiparticle system, antinodal quasiparticles with $\omega < \Delta_0$ do not exist; the typical or “on-shell” lifetime of an antinodal excitation is discussed below.) The ω^3 dependence of the inelastic scattering for nodal quasiparticles can be understood as a combination of the Fermi-liquid like ω^2 dependence and the linear ω dependence of the d -wave density of states. At higher energies, on the other hand, the broadening of the antinodal states in the case of weaker interactions (Fig. 5 (a) and (b)) becomes somewhat larger than that of the nodal states, due to the crossover to the normal state band structure. In Fig. 5 (b) we have compared the energy dependence at the node and antinode with the Fermi surface average, which will be useful to us below. It is worthwhile noting at this stage that the full Brillouin zone average of $\Gamma_{\text{inel}}(\mathbf{k}, \omega)$ (not shown) does not differ qualitatively from the Fermi surface average.

Within the generalized RPA spin fluctuation approach to the Hubbard model, it has been known for some time that if \bar{U} is adjusted to tune the system closer to the

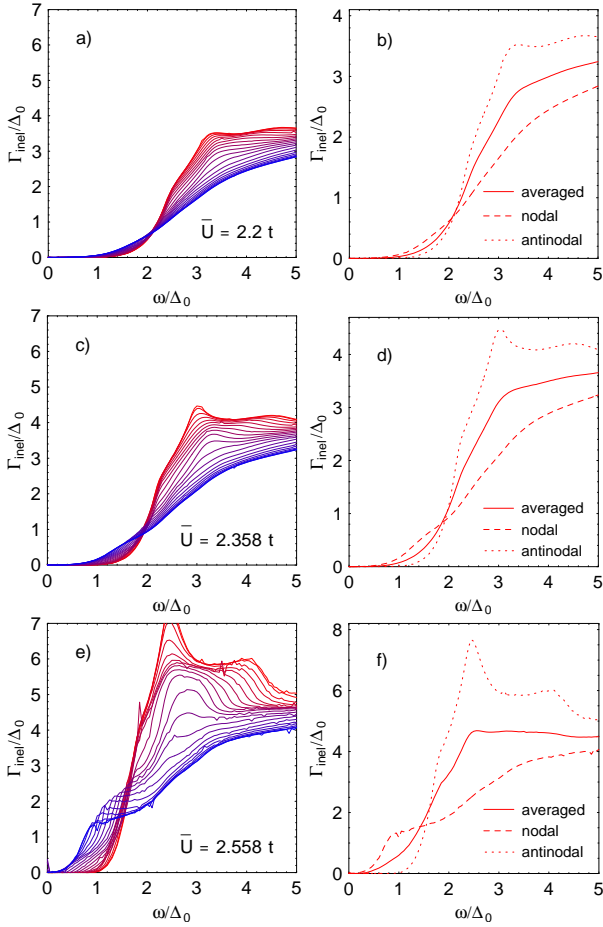


FIG. 5: (Color online) The inelastic scattering rate $\Gamma_{\text{inel}}(\mathbf{k}, \omega)$ for \mathbf{k} on the Fermi surface as a function of the quasiparticle energy ω for different values of interaction parameter $\bar{U} = 2.20t$ (a,b); $2.36t$ (c,d); and $2.56t$ (e,f). Left panels: scattering rate at different \mathbf{k} ranging in equal increments along Fermi surface from node (blue) to antinode (red). Right panels: The solid lines show the scattering rate averaged over the Fermi surface, while the dashed and dotted lines show the scattering rate for quasiparticles at the nodal and antinodal point of the Fermi surface respectively. A constant broadening of $0.1\Delta_0$ has been added to regularize the numerical calculation.

antiferromagnetic phase transition, a resonant $S = 1$ collective mode is pulled down below the particle-hole continuum in the dynamical spin susceptibility $\chi''(\mathbf{q}, \omega)$ near $\mathbf{q} = (\pi, \pi)$. This mode has been identified as the sharp spectral feature observed in neutron scattering measurements at this wavevector [33]. The RPA represents one of several approaches which have been proposed to describe the π -resonance which is observed in the cuprates [34]. Specific applications to the neutron response of different cuprate materials have been given in Ref. [35].

Here we first discuss the basic kinematics of the collective mode and consider the effect on the fermionic one-particle self-energy within our model. This has been considered already using approximate models for the suscep-

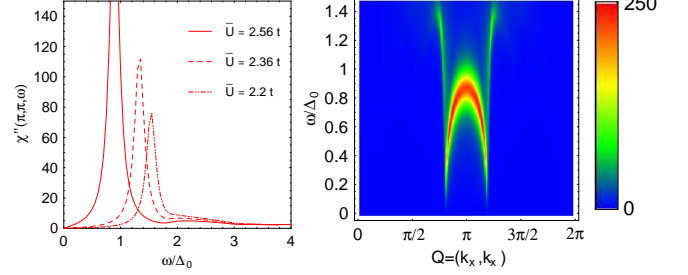


FIG. 6: (Color online) Left: imaginary part of dynamical susceptibility $\chi''(\mathbf{q}, \omega)$ vs. ω for the three values of \bar{U} considered in the text. Right: false color plot of $\chi''(\mathbf{q}, \omega)$ for a cut through the Brillouin zone along (110) .

tibility [36, 37, 38, 39] for purposes of comparing features of the neutron and ARPES spectra. Within the RPA form Eq. 17, a resonance in the real part of the susceptibility may occur when

$$\bar{U} = 1/\chi_0(\mathbf{Q}, \omega_{res}). \quad (18)$$

For our band parameters, and if we require $\mathbf{Q} = (\pi, \pi)$, the resonant frequency occurs at $\omega_{res} = 0.9\Delta_0$ for $\bar{U} = 2.56$. More generally, for \mathbf{Q} sufficiently close to (π, π) , it may be shown that $\chi''_0(\mathbf{Q}, \omega_{res})$ vanishes at $T = 0$. In this case there is a sharp collective mode contribution of the form

$$\chi''_{res}(\mathbf{Q}, \omega) = \frac{\pi}{\bar{U}} \delta(1 - \bar{U}\chi'_0(\mathbf{Q}, \omega)) \quad (19)$$

to the imaginary part of the spin susceptibility near \mathbf{Q} . In Figure 6, we show how, with increasing interaction strength, the energy position of the collective feature in χ'' shifts downward and the intensity increases. These aspects of the spin fluctuation spectrum are then directly reflected in Fig. 5. Many of the features of the experimental neutron spectrum on optimally doped YBCO[41] and BSCCO[42], including the hourglass-like shape of the neutron response in \mathbf{q}, ω space (Fig. 6 (b)), as well as characteristic rotation of the pattern of incommensurate \mathbf{q} -peaks as the energy is tuned through the resonance are known to be captured by this type of theory [34, 40].

To see how the collective mode affects the quasiparticle scattering rate, we focus on the resonant part of χ'' . The contribution to the effective interaction $V_{res}(\mathbf{q}, \omega)$ is $\frac{3}{2}U^2\chi''_{res}(\mathbf{q}, \omega)$, giving rise to an additional contribution to the total scattering rate

$$\Gamma_{res}(\mathbf{k}, \omega) = -\frac{1}{2} \sum_{\mathbf{k}', s=\pm} \text{Im} V_{res}(\mathbf{k} - \mathbf{k}', \omega + sE_{\mathbf{k}'}) \quad (20)$$

$$\times (f(sE_{\mathbf{k}'}) + n(\omega + sE_{\mathbf{k}'})) \left[1 - s \frac{\epsilon_{\mathbf{k}}\epsilon_{\mathbf{k}'} + \Delta_{\mathbf{k}}\Delta_{\mathbf{k}'}}{\omega E_{\mathbf{k}'}} \right].$$

At the node $\mathbf{k} = \mathbf{k}_N$, the expressions simplify considerably and we find at $T = 0$ that

$$\Gamma_{res}(\mathbf{k}_N, \omega) \simeq \frac{3\pi U^2}{4\bar{U}} \sum_{\mathbf{k}'} \delta(1 - \bar{U}\chi'_0(\mathbf{k} - \mathbf{k}', \omega - E_{\mathbf{k}'})) \times \theta(\omega - E_{\mathbf{k}'}). \quad (21)$$

The integrand contributes provided $\omega = \omega_{res} + \sqrt{\epsilon_{\mathbf{k}'}^2 + \Delta_0^2}$, with $\mathbf{k}' = \mathbf{k} - \mathbf{Q}$. Since for our band parameters $\mathbf{k}' = \mathbf{k}_N - (\pi, \pi)$ is far from the Fermi surface, the contribution to Γ from the magnetic resonance mode will arise at frequencies $\omega = \omega_{res} + |\epsilon_{\mathbf{k}'}|$ larger than ω_{res} itself by an amount which is of order a fraction of the Fermi energy, much larger than Δ_0 .

For the antinodal points, or rather the nearby ‘‘hot spots’’ \mathbf{k}_{HS} where the Fermi surface crosses the antiferromagnetic zone boundary, the wave vector $\mathbf{k}' = \mathbf{k}_{HS} - (\pi, \pi)$ is also on the Fermi surface. However the off-diagonal parts of the coherence factors must now also be included, so the resonant contribution becomes

$$\Gamma_{res}(\mathbf{k}_N, \omega) \simeq \frac{3\pi U^2}{4\bar{U}} \sum_{\mathbf{k}'} \delta(1 - \bar{U}\chi'_0(\mathbf{k} - \mathbf{k}', \omega - E_{\mathbf{k}'})) \times \theta(\omega - E_{\mathbf{k}'}) \left[1 - \frac{\Delta_{HS}}{\omega} \right], \quad (22)$$

where $\Delta_{HS} \approx \Delta_0$ is the value of the order parameter at the hot spot \mathbf{k}_{HS} . Thus there is a contribution to the resonant part of the scattering rate at the hot spot when $\omega \simeq \omega_{res} + \Delta_0$. This additional scattering has been claimed to be responsible for part of the ‘‘peak-dip-hump’’ structure seen in ARPES near the antinode at low temperatures in the superconducting state [36, 38]. However, since ω_{res} is also of order Δ_0 , it does not appear as though the resonant electron-electron scattering can by itself play a significant role in the electronic scattering rate for energies at or below the coherence peak energy Δ_0 .

Nevertheless, the enhanced inelastic scattering will play a role in measured STS properties. The tuning of the system closer to the antiferromagnetic instability has the effect of enhancing the overall scattering rate, such that the states near the nodes now decay more rapidly. In Figure 5(c)-(f), we show the evolution of the energy-dependent scattering rate for states along the Fermi surface for slightly larger \bar{U} . The contribution of the collective mode is easiest to discern in (e)-(f), for the case $\bar{U} = 2.56$. The scattering in the midgap range near the node has risen considerably, although near the antinode it is still exponentially suppressed at low energies. The collective mode results in a contribution which rises near $\omega \simeq \omega_{res} + \Delta_0 \approx 1.9\Delta_0$ at the antinode, as expected from the above discussion, which then peaks at about $2.5\Delta_0$. There is no obvious resonant contribution at higher energies in the nodal direction, but its existence can be deduced by considering the evolution of the antinodal peak as one moves away from the antinode: as seen in the figure, it moves to higher energies as expected and broadens due to the additional decay channels. Above

an energy of order $1.5\Delta_0$, the antinodal scattering rate is seen to become much larger than the nodal scattering rate. This enhancement is directly related to the opening of the superconducting gap and the creation of the resonant mode.

The intermediate case $\bar{U} = 2.36$ (Fig. 5(c)-(d)) also shows clear evidence of enhanced interactions, and vestiges of the mode features. The effect on Γ_{inel} at low energies is primarily quantitative: the inelastic scattering near the node becomes significant in the midgap range compared to the weaker case (a)-(b), and is already a fraction of Δ_0 near the node at the gap frequency $\omega = \Delta_0$. This will play a role in our discussion of STS experiments, because the extracted quasiparticle scattering rate is of this order for optimally doped samples. There is further independent evidence in the work of Fauqué et al. [42] to suggest that the intermediate interaction strength case we considered here is most relevant for experiments on optimally doped BSCCO. This is because in Ref. [42], the collective mode energy is measured to be 42 meV, while the average gap is extracted as 35 meV. This ratio of about 1.2 is achieved in our model for interaction strength $\bar{U} = 2.36$; changing this parameter moves the resonance up or down relative to the gap edge, as seen in Fig. 6(a).

D. Total scattering rate

To include both elastic and inelastic scattering effects, we neglect interference processes between electron-electron collisions and impurity scattering entirely, and approximate the total scattering rate by

$$\Gamma_{tot} = \Gamma_{el} + \Gamma_{inel}. \quad (23)$$

In Fig. 7, the total scattering rate for quasiparticles at the nodal point of the Fermi surface (dashed) is compared to the scattering rate for quasiparticles at the antinodal point of the Fermi surface (dotted) as well as the average scattering rate including only the quasiparticles at the Fermi surface,

$$\Gamma_{avg}(\omega) = \langle \Gamma_{tot}(\mathbf{k}, \omega) \rangle_{FS}, \quad (24)$$

where $\langle \rangle_{FS}$ is a Fermi surface average. The total scattering rate is seen in Fig. 7 (a)-(b) to be dominated for $\omega \lesssim 2\Delta_0$ by the linear energy dependence of the elastic part, while at higher energies $\omega > 3\Delta_0$ it reflects the quasilinear energy dependence of the inelastic scattering rate in the classical regime. The slope for low energies and the slope for high energies are not related to each other and depend on the individual parameters used in the two models.

For completeness, in Fig. 7 (b) the total scattering rate averaged over the Fermi surface is shown together with its two averaged contributions from elastic and inelastic scattering processes. It shows qualitatively the same energy dependence as the Brillouin zone averaged rate (not

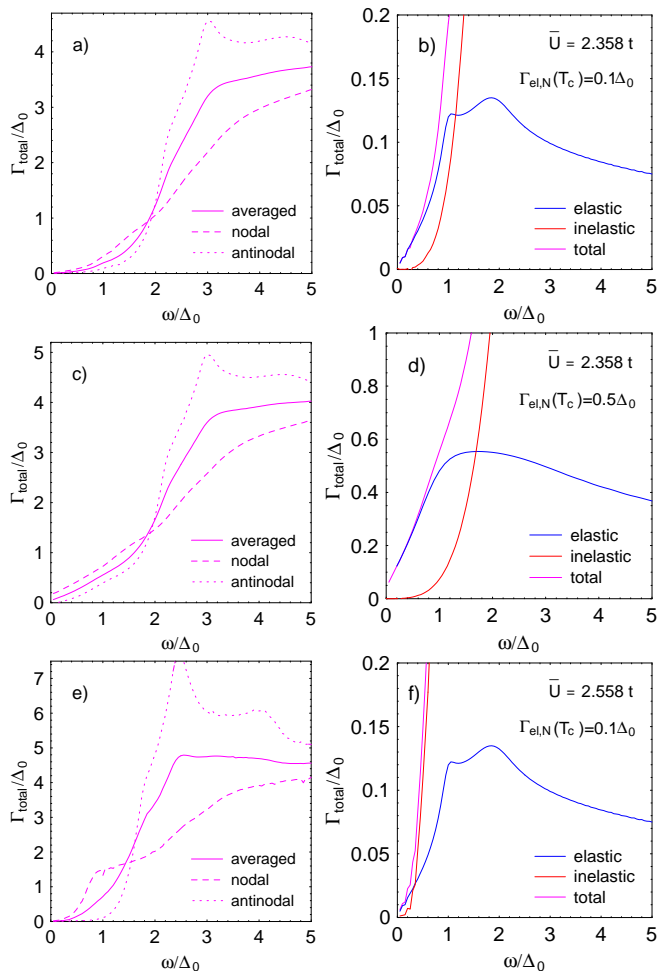


FIG. 7: (Color online) The elastic, inelastic, and total scattering rates as a function of the quasiparticle energy ω for several assumptions about the strength of each scattering channel. In the left panels, the total rate Γ_{tot} at the antinode \mathbf{k}_A (node \mathbf{k}_N) is plotted as a dotted (dashed) line. The average over the Fermi surface of $\Gamma_{tot}(\mathbf{k}, \omega)$ is plotted as the solid line. In the right panels, the contribution of the elastic (blue) and inelastic (orange) to the total (magenta) Fermi surface averaged rates is exhibited separately. (a)-(b) are for the case $\bar{U} = 2.36t$ with $\Gamma_{el,N}(T_c) = 0.1\Delta_0$. (c)-(d) Same as (a)-(b) but with $\Gamma_{el,N}(T_c) = 0.5\Delta_0$. (e)-(f) Same as (a)-(b) but with $\bar{U} = 2.56t$.

shown) but has a somewhat larger overall magnitude. This is due to the fact that the Brillouin zone average includes regions of the zone away from the Fermi surface with small scattering rates.

IV. LOCAL GREEN'S FUNCTION

In this section we calculate the exact local Green's function including impurity and spin-fluctuation scattering, and exhibit the LDOS for varying amounts of disorder and different interaction strengths. Our first goal

is to see if the use of a local self-energy, which we define in an ad hoc way, can provide a good description of the exact LDOS calculated with the full self-energies. Secondly, we compare these approximations to the linear- ω ansatz, given by Eqs. 1-2, employed by the Cornell group to fit their data [8]. We would like to see if an approximate local self-energy may be constructed from the local Green's function, and to what extent the true self-energy yields an LDOS similar to that obtained from the linear- ω scattering rate.

The local Green's function $\underline{G}(\mathbf{r}, \mathbf{r}, \omega)$ in the presence of elastic and inelastic scattering is given, within a region of size of order ℓ , as the Fourier transform of the momentum dependent Green's function $\underline{G}(\mathbf{k}, \omega)$

$$\underline{G}(\mathbf{r}, \mathbf{r}, \omega) = \sum_{\mathbf{k}} \underline{G}(\mathbf{k}, \omega) \quad (25)$$

Here the full momentum dependent Green's function is calculated from

$$\underline{G}(\mathbf{k}, \omega) = \frac{\tilde{\omega}\tau_0 + \tilde{\epsilon}_{\mathbf{k}}\tau_3 + \tilde{\Delta}_{\mathbf{k}}\tau_1}{\tilde{\omega}^2 - \tilde{\epsilon}_{\mathbf{k}}^2 - \tilde{\Delta}_{\mathbf{k}}^2} \quad (26)$$

and $\tilde{\omega}$, $\tilde{\epsilon}_{\mathbf{k}}$ and $\tilde{\Delta}_{\mathbf{k}}$ are the renormalized quasiparticle energy, band structure and gap in the presence of the elastic and inelastic self-energy calculated in the previous section. The LDOS is then simply given by

$$N(\mathbf{r}, \omega) = -\frac{1}{2\pi} \text{Tr} [(\tau_0 + \tau_3)\underline{G}(\mathbf{r}, \mathbf{r}; \omega)]. \quad (27)$$

The results of these calculations including the full self-energies are shown as the solid lines in Fig. 8 for (a) pure elastic scattering, (b) pure inelastic scattering and (c) for the total scattering rate. The green curve shows for comparison the the LDOS for a clean d -wave superconductor. The high slope of the elastic scattering rate leads to a linear energy dependence of the total rate up to a value of Δ_0 and a strong suppression of the coherence peaks. The inelastic scattering rate, which is strongly suppressed for low energies, begins to significantly affect the LDOS only at energies $\omega \gtrsim \Delta_0$ for the slightly off-resonant case $\bar{U} = 2.36t$ case shown, and has qualitatively no influence on the low energy spectrum. In the same figure panels, we compare these results to calculations with the ad hoc "local" scattering rate $\Gamma_{avg}(\omega)$ which we simply add as an imaginary part to the quasiparticle energy,

$$\underline{G}[\mathbf{r}, \mathbf{r}, \omega + i\Gamma_{avg}(\omega)] = \sum_{\mathbf{k}} \underline{G}[\mathbf{k}, \omega + i\Gamma_{avg}(\omega)]. \quad (28)$$

As can be seen, this approximation (dashed lines) leads to a slightly lower spectral weight for low energies but exhibits also a quasilinear energy dependence for the local density of states up to an energy of Δ_0 . Finally we fit the effective momentum averaged scattering rate with the linear energy dependence of Eq. 2 and we find for low energies excellent agreement with the approximation of a momentum averaged scattering rate (orange).

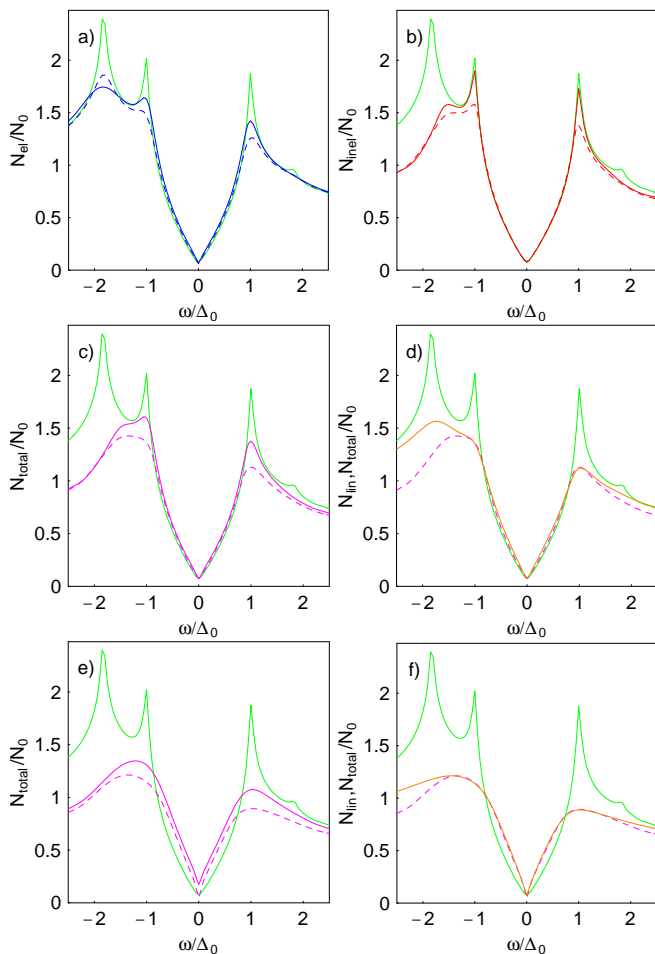


FIG. 8: (Color online) The local density of states (LDOS) $N_{\text{total}}(\omega)$ normalized to the Fermi level density of states N_0 for a d -wave superconductor with scattering processes of various types included. In all panels, green line shows LDOS for pure system, blue (a) gives the LDOS for pure elastic scattering with $\Gamma_{\text{el}}(T_c) = 0.1\Delta_0$, red curve (b) gives pure inelastic scattering with $U = 2.36$, and magenta (c) includes both elastic and inelastic processes. Solid lines are calculated with the full momentum dependent self-energy, while the dashed curves used an effective momentum averaged scattering rate defined in (24). In (d) the LDOS in the presence of impurity and spin fluctuation scattering, with parameters from (a) and (b), is compared to the best fit $N_{\text{lin}}(\omega)$ (orange) using a linear scattering rate of the form given in Eqs. (1-2) as extracted from STS data in Ref. 8. Figs. (e) and (f) show the LDOS for a dirtier system with $\Gamma_{\text{el}}(T_c) = 0.5\Delta_0$ (line types same as in (a)-(d)).

Thus we conclude that for energies $\omega \lesssim \Delta_0$, there is a quasilinear increase of Γ arising from elastic scattering processes and in calculating the LDOS it can be modeled by the linear form Eq. (2). On the other hand, the STS local scattering rate is also enhanced by inelastic scattering processes when $\omega \gtrsim \Delta_0$. Despite the fact that this destroys even the approximate linearity of the total scattering rate (see Fig. 7), the momentum average in-

herent in the local measurement implies that it is very difficult to distinguish the true functional form of Γ in the impurity plus spin fluctuation model from the phenomenological linear ansatz of Ref. [8]. We return to this point in Section V below.

The results in Fig. 8 are qualitatively similar to earlier attempts to fit STS data by assuming a model self-energy dressing a BCS-like d -wave Green's function. In particular, Hoogenboom et al. [43] and de Castro et al. [44] compared data on BSCCO to self-energy models with constant scattering rates, a marginal Fermi liquid model [45], and the model of Ref. [38] describing a coupling to a phenomenological collective spin mode. They concluded that details of the peak-dip-hump structure observed in some spectra required the collective mode, and identified features at sum and difference energies of the gap and collective mode frequency. Here we have attempted no detailed fits of STS data, as we are primarily interested in exploring the general notion of a local scattering rate. We note that Fig. 8 shows, as in Refs. [43, 44], the broadening of the van Hove singularity by inelastic scattering, and that out-of-plane elastic scattering may play a role as well. Peak-dip-hump structures similar to experiment are seen in some cases in Fig. 8, but more investigation is needed to determine whether these aspects of the experimental spectra correspond to scattering effects of the type considered here.

V. COMPARISON WITH ARPES SPECTRAL FUNCTION

The model of the quasiparticle scattering rate put forward above has implications for other quantities besides the STS conductance, and we may learn something from the comparison. In particular, as mentioned in the introduction, ARPES has reported superconducting state relaxation rates which are many times larger than those measured by STS. A naive application of these ARPES rates in the superconducting state would lead to even broader LDOS spectra than those in Fig. 8(e)-(f), in contradiction to experiment. The ARPES signal is given in the sudden approximation by

$$I(\mathbf{k}, \omega) = |M|^2 A(\mathbf{k}, \omega) f(\omega), \quad (29)$$

where M is an ARPES matrix element, which we take to be constant, $A(\mathbf{k}, \omega) = -(1/2\pi)\text{Im Tr}(\tau_0 + \tau_3)\underline{G}(\mathbf{k}, \omega)$, and f is the Fermi function. Here we calculate the full electron spectral function $A(\mathbf{k}, \omega)$ within our simple model, for different points on the Fermi surface and for different scattering rates, with the aim of describing some qualitative phenomena and comparing with STS. We note that the Fermi surface itself is, in the presence of interactions and scattering, not identical with the non-interacting pure one, but rather is the solution in \mathbf{k} space of the equation

$$\text{Re } \tilde{\epsilon}_{\mathbf{k}} = \epsilon_{\mathbf{k}} + \text{Re}(\Sigma_3^{\text{el}} + \Sigma_3^{\text{inel}}) = 0. \quad (30)$$

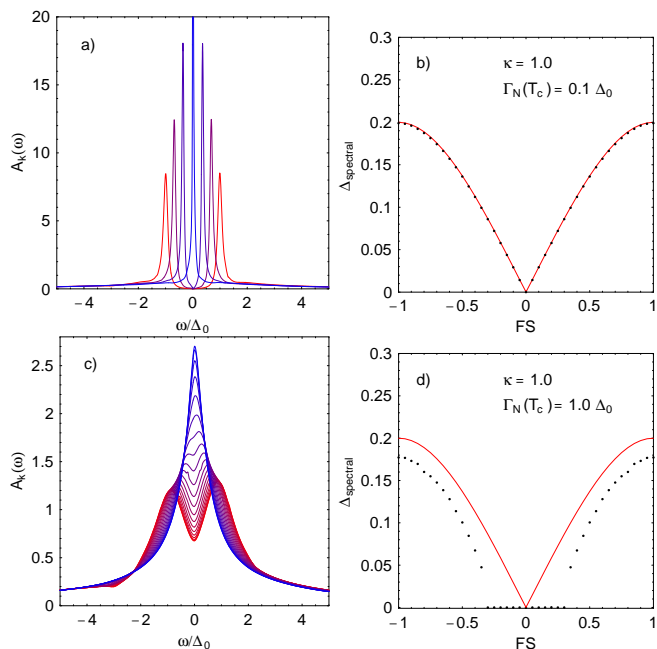


FIG. 9: (Color online) Left: spectral function $A(\mathbf{k}, \omega)$ for \mathbf{k} on the Fermi surface at $T = 0$ with elastic scattering parameters $\kappa = 1$ and (a) $\Gamma_{el,N}(T_c) = 0.1\Delta_0$ and (c) $\Gamma_{el,N}(T_c) = \Delta_0$, and with the inelastic scattering rate calculated with $\bar{U} = 2.36t$. Color ranges in equal increments from blue (node) to red (antinode). Only four \mathbf{k} points are shown in (a) due to narrowness of peaks. Right: spectral gap as determined by one-half the energy difference between the two maxima of $A(\mathbf{k}, \omega)$ for (b) $\Gamma_{el,N}(T_c) = 0.1\Delta_0$ and (d) $\Gamma_{el,N}(T_c) = \Delta_0$, respectively. Red curve in both figures indicates pure d -wave gap in the absence of scattering.

Here the chemical potential is determined to maintain a given filling. We have verified that this does not affect the broadening and in the calculation of the spectral functions shown in Fig. 9 the renormalization of the Fermi surface by $\text{Re } \Sigma$ was neglected.

In Fig. 9 (a),(c), we show the evolution of the low-temperature spectral function along the Fermi surface, beginning with the (blue) peak centered at $\omega = 0$ as expected, and ending with two clear (red) peaks at the antinode. Close to the node, some spectra still have their maxima at the Fermi surface due to scattering effects. In the pseudogap state of the cuprates, a similar phenomenon is observed: the maximum of the spectral function remains at the Fermi surface over some range of \mathbf{k} values centered on the nodal point; the pseudogap itself is visible as a double-peak structure only some distance away from the nodal point. The range of \mathbf{k} where the single maximum is at the Fermi energy is called the Fermi “arc”, and it evolves continuously into the full Fermi surface in the normal state as the pseudogap disappears. It has been pointed out by several authors [5, 6, 7] that the arc phenomenon can be explained trivially by appealing

to an energy and/or temperature-dependent scattering rate, which for sufficiently large scattering broadens the two-peak spectral function one would expect in the presence of a spectral gap into a single peak centered at the Fermi level. A similar phenomenon occurs here in the superconducting state, as shown in Fig. 9 (b),(d), where the effective gap, determined from the position of the spectral function peak, is plotted along the Fermi surface, exhibiting a finite range of \mathbf{k} points where it vanishes. For a constant scattering rate Γ , the criterion determining the angular position of the end of the arc is $\Gamma = a\Delta_{\mathbf{k}}$, where a is a constant of order unity, equal to $\sqrt{3}$ for a d -wave superconductor with circular Fermi surface and $\cos 2\phi$ order parameter[7]. Note the effective gap determined by ARPES in this manner does not correspond to the renormalized order parameter in the theory, as pointed out by Sensarma et al. [46].

Since the scattering rate is temperature and frequency dependent, the criterion for the position of the spectral peaks changes as T is increased, resulting in a temperature-dependent change in the “arc length”, as shown in Fig. 10. This is a very weak temperature dependence until quite close to T_c , since it is driven by the T -dependence of the gap in the theory [19], and above T_c the arc length in the current model is fixed because the gap goes to zero. A theory including a pseudogap in the normal metallic dispersion would give rise to a T -dependent (linear- T for a marginal Fermi liquid-like scattering rate[45]) arc length [5, 6, 7]. Here we have shown that, at low T in the superconducting state, Fermi arcs are also possible, but only in a dirty system. Thus the recent observation by Kanigel et al. [47] of the collapse of the arc length at low T in the superconducting state places constraints on the elastic scattering rate. Since no arc is observed at low T in optimally doped samples, the scattering rate must be a tiny fraction of Δ_0 , inconsistent with ARPES determinations of such rates at low T , but consistent with the STS result[8] of $\Gamma(\omega \simeq \Delta_0) \sim 2$ meV near optimal doping. On the other hand, STS has shown that the linear fits to the scattering rate yield a tenfold increase in this rate for highly underdoped samples. In this case, Γ becomes an appreciable fraction of Δ_0 for subgap energies. The implication is therefore clear that ARPES should eventually observe arcs in the superconducting state as the system is underdoped.

Finally, it is worth observing that in Fig. 9 (a),(c) the EDC width at the antinodal points is significantly larger than at the antinode in the clean case shown in 9(a)), despite the fact that the antinodal scattering rate does not exceed the nodal one until energies several times Δ_0 . This is primarily because the EDC’s are dominated by quasiparticles “on the mass shell” $\omega = \Delta_{\mathbf{k}}$. Thus, while the nodal scattering rate is actually larger than the antinodal scattering rate for $\omega = \Delta_0$, as shown in Fig. 7, the scattering rates which broaden $A(\mathbf{k}, \omega)$ are associated with on-shell $\omega = \Delta_{\mathbf{k}}$ energies. In this case, the antinodal scattering rate refers to quasiparticles of en-

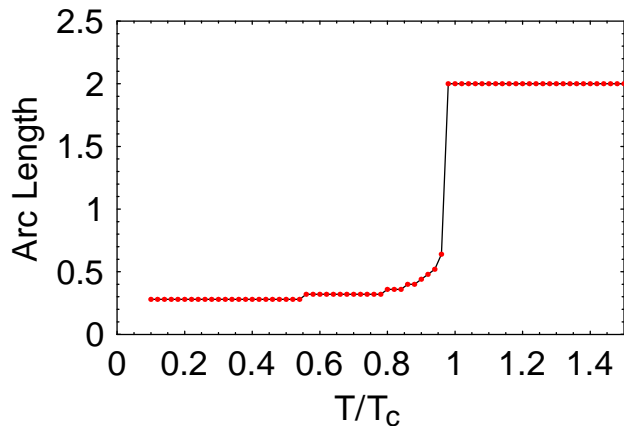


FIG. 10: (Color online) Length of “Fermi arc” defined in text at $T = 0$ in superconducting state vs. temperature T/T_c . Elastic scattering rate parameter $\Gamma_{el,N} = \Delta_0$

ergy $\omega \sim \Delta_0$, while the nodal scattering rate to those of energy $\omega \sim 0$. In addition, if interactions are sufficiently strong, the inelastic scattering at the antinode will eventually contribute, leading to a pronounced asymmetry of the spectral function in the form of a large tail on the high binding energy side in ARPES. This may contribute significantly to measured EDC widths if electron-electron scattering is sufficiently strong.

VI. EFFECT OF SAMPLE INHOMOGENEITY

A. Low energy homogeneity

Thus far we have considered a homogeneous d -wave superconductor with inelastic scattering and microscopic disorder, which we treated by averaging to obtain a translationally invariant self-energy characterized by momentum \mathbf{k} . We saw in the previous section that at a given quasiparticle energy, calculating a “local self-energy” $\sum_{\mathbf{k}} \Sigma(\mathbf{k}, \omega)$ provided a reasonable description of the LDOS broadening. This assumes, as discussed in the introduction, that the system is self-averaging within a region with a single gap magnitude $\Delta_{\mathbf{k}}$. However, the BSCCO-2212 system is known to be inhomogeneous at the nanoscale, in a somewhat mysterious way. Spectra measured near the typical gap edge of a given sample are extremely inhomogeneous, with coherence peak positions varying up to a factor of 2-3 within a typical experimental field of view. On the other hand, below some typical energy of order 30 meV, near-homogeneity is recovered [24].

Let us consider the STM-determined low-energy local scattering rates. These are quite small relative to rates determined by ARPES, but increase with increasing energy. It is our hypothesis that quasiparticles at low energy scatter so seldom that they explore many gap “patches”, and thus do *not* carry knowledge of the lo-

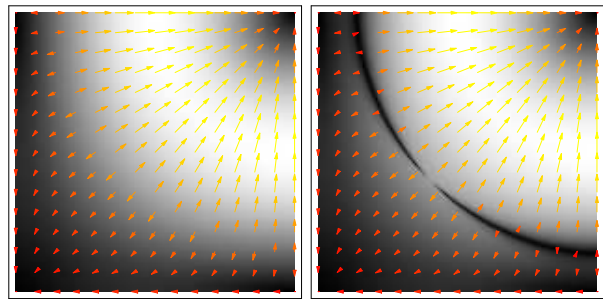


FIG. 11: (Color online) Quasiparticle group velocity for band structure given in (12) for a) normal state; b) superconducting state. Length of arrows or grayscale indicate size of local quasiparticle speed.

cal gap value when collected by the STM tip. As the energy increases, eventually their mean free path drops until they are localized within a single patch. Conductance spectra taken at these higher energies will therefore reflect the local gap at the position of the STM tip. It is significant (a) that the energy where inhomogeneity appears is of order Δ_0 in Bi-2212, and b) that the doping dependence of this energy scale is rather weak.

To calculate the energy-dependent mean free path of our system, we will need the velocity of a typical Bogoliubov quasiparticle \bar{v}_{qp} at different points near the Fermi surface at $T = 0$. The group velocity for a quasiparticle of momentum \mathbf{k} in a clean BCS superconductor is $v_{\mathbf{k}} \equiv \nabla E_{\mathbf{k}}$. Here however we are accounting for scattering of these quasiparticles by impurities and collisions; therefore there is an effective spread in momentum of a typical quasiparticle due to its lifetime broadening. We therefore define the speed of a typical quasiparticle near the Fermi surface with momentum $\mathbf{k} = (k_{\perp}, k_{\parallel})$ and energy at the gap edge to be

$$\bar{v}_{k_{\parallel}} = \sqrt{\sum_{k_{\perp}} v_{\mathbf{k}}^2 A(\mathbf{k}, \omega = \Delta_{\mathbf{k}})} \quad (31)$$

At the node, the spectral function is (neglecting real parts of self-energies) $A(\mathbf{k}_N, \omega) \simeq (\Gamma/\pi)/(\xi^2 + \Gamma^2)$, so using (31) we find $\bar{v}_{qp}(\mathbf{k}_N) = v_F(\mathbf{k}_N)$. At the antinode, the spectral function is approximately

$$A(\mathbf{k}_A, \omega) \simeq \frac{\Gamma}{\pi} \frac{2\Delta_0(\Delta_0 + \xi)}{\xi^4 + 4\Delta_0^2\Gamma^2}, \quad (32)$$

leading to

$$\bar{v}_{qp}(\mathbf{k}_A) \approx \sqrt{\frac{2\Gamma}{\Delta_0}} v_F(\mathbf{k}_A), \quad (33)$$

where we have assumed $\Gamma \ll \Delta_0$. Thus the “typical” antinodal velocity is generally much smaller than the normal state Fermi velocity. Using the STM determined value of $\Gamma = 2$ meV at optimal doping, \bar{v}_{qp} should be

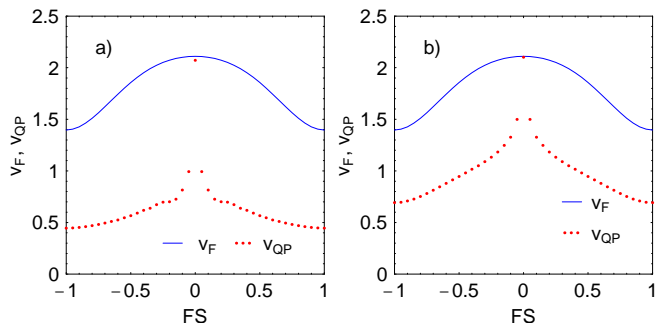


FIG. 12: (Color online) Typical quasiparticle group velocity for band structure given in (12) vs. position on Fermi surface using expression (31). The inelastic scattering is calculated for $\bar{U} = 2.36t$ while the elastic scattering corresponds to $\Gamma_N(T_c) = 0.05\Delta_0$ (a) and $\Gamma = 0.2\Delta_0$ (b).

suppressed by a factor of 3-4 relative to the Fermi velocity. This is confirmed by a full evaluation of (31) using the self energy given by Eq. 23.

We now define the on-shell quasiparticle mean free path

$$\ell_{\mathbf{k}} \equiv \frac{\bar{v}_{qp}}{2\Gamma(\omega = \Delta_{\mathbf{k}})}, \quad (34)$$

where Γ may represent the elastic, inelastic, or total one-particle scattering rate. For extremely dirty systems, momentum is not a good quantum number, and the on-shell quantities may not provide a good representation of the mean free path. However for the doped cuprate samples of interest it appears to us that this is a reasonable estimate. The on-shell scattering rate is precisely that defined for the ω -dependent momenta \mathbf{k} corresponding to the points of the contours of constant quasiparticle energy $E_{\mathbf{k}}$ which lie on the Fermi surface, i.e. the so-called ‘‘banana tips’’ defined within the octet model[48]. In Fig. 13, we plot both the scattering rates and mean free paths defined in this way. These are shown both as a function of ω and, equivalently, of \mathbf{k} , for the set of parameters corresponding to a clean system with inelastic scattering rate parameter $U = 2.36t$ consistent with neutron data, as in Fig. 7 (a) and (b) and Fig. 8 (a) and (b). In Fig. 13 (a) and (b), we see that the effective on-shell scattering rate is indeed quasi-linear in energy over the range $0 < \omega \lesssim \Delta_0$, resulting in a momentum dependence similar to the d -wave gap itself. The parameters chosen to approximately reproduce the neutron scattering behavior in YBCO (Fig. 7 (a)-(b)) appear to give a scattering rate scale of approximately $0.1\Delta_0$, of order the correct scale of 2meV determined by STS for BSCCO.

The mean free path in Fig. 13 is seen to fall rapidly with increasing energy, and becomes of order the patch size $\sim 10a$ at an energy around the gap edge. We will designate this energy ω_{loc} since it is only above this energy where true local behavior characteristic of a particular

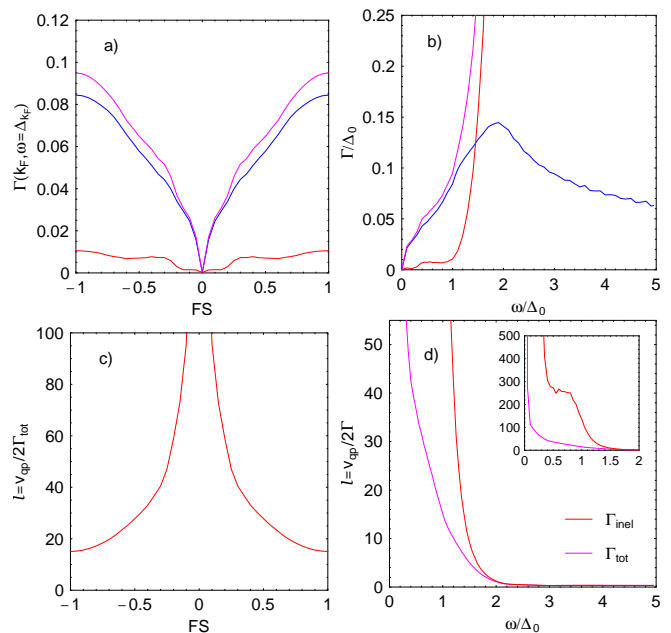


FIG. 13: (Color online) (a) on-shell scattering rate $\Gamma_{\text{tot}}(\mathbf{k}, \omega = \Delta_{\mathbf{k}})$ as a function of \mathbf{k} from the node to the antinode along the Fermi surface parameterized from -1 to 1, for scattering parameters elastic scattering parameters $\kappa = 1$, $\Gamma_{\text{el}}(T_c) = 0.1\Delta_0$ and $\bar{U} = 2.36t$. Blue: elastic scattering; red: inelastic; magenta: total scattering rate. (b) same quantity plotted vs. ω . (c,d) Mean free path $\ell \equiv v_{qp}/(2\Gamma_{\text{tot}}(\mathbf{k}, \omega = \Delta_{\mathbf{k}}))$ vs. \mathbf{k} and ω as in (a,b).

gap patch order parameter is measured. This is reminiscent of the behavior identified by STS on BSCCO-2212 samples: below a critical energy ω_{loc} of order or slightly less than Δ_0 , spectra are homogeneous. The famous inhomogeneity measured by STS in this system appears only above this energy, and in particular at and around the average gap energy (and above for underdoped samples). The energy ω_{loc} above which the sample inhomogeneity is sensed by the STS measurement is therefore where spectra measured in different locations begin to differ from one another, and must therefore necessarily be associated with a change in slope $N(\omega)$ at ω_{loc} . Such a kink in typical spectra where homogeneity is lost has indeed been observed in STS data [24, 49].

We note also the relative insensitivity of the observed kink energy to doping p [50], despite rapid changes in both the scattering rate and gap size over the measured range of $p \simeq 0.08 - 0.2$. Within our picture, this can be understood at least in part by the increase of the antinodal typical quasiparticle velocity with the scattering rate as shown in Eq. (33). Changes in Fermi surface shape may also play a role in keeping the mean free path at this energy roughly doping independent.

Finally, we comment on the significance of these results for the quasiparticle interference (QPI) patterns observed in Fourier transform STS on these systems[48]. It is important to recall that the QPI patterns arise due to the

random static potential from impurities. Static disorder can enhance noise which may then swamp certain Fourier transform \mathbf{q} -peaks[51], but it cannot suppress or broaden those peaks in \mathbf{q} -space. Inelastic scattering however will dephase quasiparticle wavefunctions, and it is to be expected that a given FT-STs \mathbf{q} -peak will be lost when the inelastic scattering rate becomes large enough such that the de Broglie wavelength of a quasiparticle at the Fermi level is smeared by a significant fraction. The theoretical question of how such quasiparticle interference patterns are destroyed is an interesting one, which we are currently studying in more detail. At present, however, our results suggest that a qualitative increase in this smearing occurs in the neighborhood of $\omega^* \sim \Delta_0$ due to the rapid rise of the inelastic scattering. It is *not* clear from our analysis that the two energy scales ω_{loc} where the system inhomogeneity becomes manifest and the scale ω^* where QPI patterns are destroyed are the same scale, but they are of the same order, and experimentally appear to be quite close[50].

B. STS and ARPES quasiparticle relaxation rates

The size of the ARPES laser spot on the sample surface is many times larger than a typical “gap patch” size in BSCCO-2212. This fact has been frequently pointed out, but its consequences for extracted quasiparticle lifetimes has not been explored to our knowledge. We noted in the introduction that ARPES-extracted lifetimes for both nodal and antinodal quasiparticles are much larger than those determined recently by STS [8]. This fact can be plausibly explained by taking our current knowledge of STS lifetimes and averaging the spectral function over the distribution of gaps $P(\Delta)$ found near the BSCCO-2212 surface. A similar analysis was performed by Fauqué et al.[42] to explain the large width of the neutron resonance peak in BSCCO-2212, assuming that the same distribution characterized the bulk of the sample probed by neutrons. The gap distribution in STS has been found to have a form roughly equal to a Gaussian centered at the average gap $\bar{\Delta}$ and having a width σ approximately equal to $0.2\bar{\Delta}$, more or less independent of doping [8]. In Alldredge et al., the STS scattering rate at the gap energy was extracted as $\sim \alpha\omega$, as described in the introduction. The average α for an optimally doped sample was $\langle \alpha \rangle \simeq 0.04$, giving a scattering rate at $\omega = \bar{\Delta} \simeq 40\text{meV}$ of $\sim 2\text{meV}$, or $0.05\bar{\Delta}$.

The spectral function at the antinode where this gap value is achieved is shown in Fig. 14 as the dashed line, a narrow Lorentzian centered at Δ_0 . But ARPES averages over many such lines, each centered at a different Δ_0 and broadened by a different scattering rate, which depends on Δ_0 in the above analysis. The solid line in Fig. 14 is then given by

$$A_{\text{ARPES}}(\mathbf{k}, \omega) \simeq \int P(\Delta_0) A(\mathbf{k}, \omega; \Delta_0), \quad (35)$$

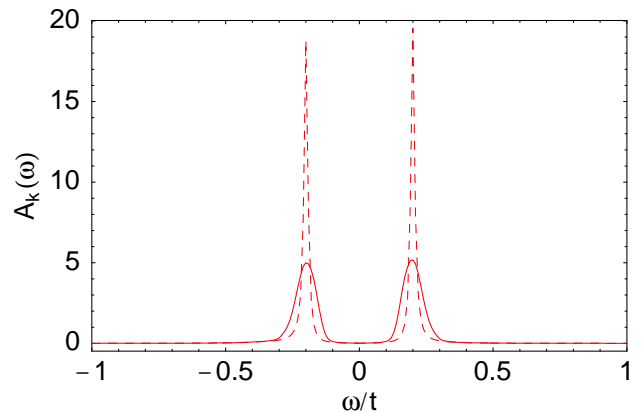


FIG. 14: (Color online) $T=0$ spectral function at antinode for homogeneous d -wave superconductor with scattering rate of $\Gamma_{\text{el}}(T_c) = 0.05\Delta_0$ (dashed lines). The solid line is the same spectral function convolved with a Gaussian distribution of gap values $P(\Delta_0)$ taken from experiment [8]. Full width at half-maximum of the solid curve is about $5\times$ that of the dashed curve. Note no instrumental energy broadening has been added to this curve.

where $A(\mathbf{k}, \omega; \Delta_0)$ is the spectral function calculated in Section V. Note to make this plot inelastic scattering was neglected in order to make the computation time practicable. However our investigations showed that the distribution of center positions (gap values) is in any case much more important for the ultimate measured EDC width than the distribution of (Δ -dependent) scattering rates. This effective spectral function is roughly five times wider than the “intrinsic” spectral function which would be measured locally in a small region where the local gap $\Delta(r)$ is $\bar{\Delta}$. Together with the instrumental resolution of ARPES near the antinode of roughly 10meV , which should be convolved with Eq. (35), this gives an effective antinodal EDC full width at half maximum of $\sim 25\text{meV}$. This is very similar to the full widths of antinodal ARPES EDC’s currently reported[4]. It therefore appears to us that the inhomogeneity effectively prevents ARPES (and planar tunnelling measurements, which suffer from the same problem) from measuring intrinsic lifetimes in the superconducting state of the BSCCO family of materials.

VII. CONCLUSIONS

In this paper we have examined a series of questions arising from recent STS measurements of lifetimes in BSCCO extracted from fits of the conductance to a BCS d -wave form with broadening, Eqs. (1) and (2). We have argued that an STS measurement probes local d -wave quasiparticle states averaged over a mean free path, with the exception of unitary bound states where quasiparticles are trapped on an atomic scale. We have discussed different mechanisms for the scattering of quasiparticles

in the superconducting state, and presented the results of model calculations within a BCS framework. Among these scattering processes are elastic quasiforward weak scattering by out of plane dopants, elastic pairing disorder scattering by the same dopants, and elastic unitary isotropic scattering by in-plane defects. We also considered the effects of inelastic scattering by spin fluctuations treated within a generalized random phase approximation, for different values of the quasiparticle interaction parameter, corresponding to a dynamical spin susceptibility at π, π with a resonant mode contribution in the d -wave state.

Within this model, the effective scattering rate rises with energy, and is generally linear at low energy due to weak elastic processes. If interactions are weak, quasiparticles over the whole “low-energy” range $\omega \lesssim \Delta_0$ are scattered primarily by impurities. If the system is sufficiently clean, or if quasiparticle interactions are sufficiently strong such as to induce a resonant mode, one may have a situation where the elastic processes dominate only up to a subgap crossover energy $\lesssim \Delta_0$. In the case with resonant mode considered in Fig. 5(e)-(f), for example, this energy was of order $0.5\Delta_0$ and the inelastic scattering rate for near-nodal states rose rapidly above this energy; weaker interactions move this crossover above the gap edge. The energy dependence of the total scattering rate for any of these situations is never strictly linear as a function of ω . However, we found that the model LDOS is well approximated by the imaginary part of a d -wave Green’s function with a linear self-energy. This was understood in terms of the effective on-shell total scattering rate, which indeed appears to be quasilinear for reasonable parameters. Therefore, while the STS extraction of local lifetimes is not particularly sensitive to the details of scattering of the low energy states, it is roughly correct and provides important insight regarding the doping dependence of local scattering.

In this work we have focussed primarily on optimal doping, where a BCS weak-coupling approach may be expected to work well. We have therefore not addressed this striking doping dependence of the STS scattering rate, where increases of a factor of ten or more relative to optimal doping were reported in strongly underdoped samples[8]. Within the present theory, such effects might be captured if the effective \bar{U}/t were to increase with underdoping, but this is difficult to describe in a systematic manner in such a framework, as is well known. In addition, we have not addressed the measured correlation of the scattering coefficient α with local gap size Δ_0 . In fact, within the description of elastic potential scattering discussed above, an anticorrelation would be obtained, in contradiction to experiment. On the other hand, pair disorder scattering, which we have also discussed briefly, appears to provide a qualitatively correct description of this empirical fact, as well as a quasilinear in ω local scattering rate. While we have not provided a consistent microscopic description of this physics, it appears to us to be worth exploring further.

As energy increases, the rising quasiparticle scattering rate leads to a falling mean free path. Our estimates show that at low energy, quasiparticles explore (and self-average over) a large area, providing an explanation of why STS spectra are homogeneous at low energies. At some critical energy ω_{loc} of order Δ_0 , the mean free path becomes of order the gap patch size, and STS then (for $\omega > \omega_{loc}$) measures spectra broadened by a local self-energy characteristic of a single gap. The fact that a change in slope in conductance spectra is observed at nearly the same energy in all patches appears to suggest that the scattering rate rises fairly rapidly in this energy range. Above this energy, conductance spectra are no longer homogeneous since self-averaging over many gap patches no longer takes place. It is furthermore to be expected—although we have not shown this directly—that dispersive quasiparticle interference patterns observed in Fourier transform STS will disappear at roughly this energy as well, since their existence depends on the assumption of a quasiparticle with definite energy scattering many times from a disorder potential.

To compare with ARPES, we have used the same model to calculate the spectral function $A(\mathbf{k}, \omega)$, and shown that a “Fermi arc”—where the spectral peak remains at the Fermi level away from the node in momentum space—may exist in the superconductin state. We argued that while current experiments on optimally doped samples do not see this feature, it should become visible in underdoped samples as scattering rates increase. Actual ARPES EDC linewidths are much broader in energy than those found within our model of a homogeneous d -wave superconductor. We have therefore argued here that this is due in large part to shifts of the spectral function caused by gap inhomogeneity, at least in the BSCCO family of cuprates, and estimated the effective EDC width which should be measured in such a system. Additional effects which add to this large enhancement of EDC linewidths include ARPES instrumental broadening and possible bilayer effects near the antinode. The current theory appears to account for the much larger ARPES EDC widths in the superconducting state compared to STS.

In this paper we have concentrated primarily on qualitative physics, leaving open questions of quantitative fits to the ARPES and STS spectra. We hope to address these in a future publication.

Acknowledgments

The authors are grateful for discussions with J. Allredge, A. Damascelli, J.C. Davis, D. Maslov and P. Wölfle. Work was begun at a workshop supported by the Aspen Center for Physics, and was partially funded by DOE Grant DE-FG02-05ER46236. DJS would like to acknowledge the Center for Nanophase Material Science at Oak Ridge National Laboratory for support.

- [1] R. Harris, P. J. Turner, Saeid Kamal, A. R. Hosseini, P. Dosanjh, G. K. Mullins, J. S. Bobowski, C. P. Bidinosti, D. M. Broun, Ruixing Liang, W. N. Hardy, and D. A. Bonn, *Phys. Rev. B* **74**, 104508 (2006).
- [2] S. Ozcan, P. J. Turner, J. R. Waldram, R. J. Drost, P. H. Kes, and D. M. Broun, *Phys. Rev. B* **73**, 064506 (2006).
- [3] T. Yamasaki, K. Yamazaki, A. Ino, M. Arita, H. Namatame, M. Taniguchi, A. Fujimori, Z.-X. Shen, M. Ishikado, S. Uchida, *Phys. Rev. B* **75**, 140513 (2007).
- [4] A. Damascelli, Z. Hussain, and Z.-X. Shen, *Rev. Mod. Phys.* **75**, 473 (2003).
- [5] J.G. Storey, J.L. Tallon, G.V.M. Williams, J.W. Loram, arXiv:0707.1549.
- [6] A. V. Chubukov, M. R. Norman, A. J. Millis, E. Abrahams, arXiv:0709.1650.
- [7] M. R. Norman, A. Kanigel, M. Randeria, U. Chatterjee, J. C. Campuzano, arXiv:0708.1713.
- [8] J.W. Alldredge, Jinho Lee, K. McElroy, M. Wang, K. Fujita, Y. Kohsaka, C. Taylor, H. Eisaki, S. Uchida, P.J. Hirschfeld and J.C. Davis, arXiv:0801.0087.
- [9] I. Martin and A.V. Balatsky, *Physica C (Amsterdam)* **357-360**, 46 (2001).
- [10] Z. Wang, J. R. Engelbrecht, S. Wang, H. Ding, and S. H. Pan, *Phys. Rev. B* **65**, 064509(R) (2002).
- [11] S. A. Kivelson, I.P. Bindloss, E. Fradkin, V. Oganessian, J.M. Tranquada, A. Kapitulnik, and C. Howald, *Rev. Mod. Phys.* **75**, 1201 (2003).
- [12] T.S. Nunner, B.M. Andersen, A. Melikyan and P.J. Hirschfeld, *Phys. Rev. Lett.* **95**, 177003 (2005).
- [13] J.-X. Zhu, arXiv:cond-mat/0508646.
- [14] A. C. Fang, L. Capriotti, D. J. Scalapino, S. A. Kivelson, N. Kaneko, M. Greven, and A. Kapitulnik, *Phys. Rev. Lett.* **96**, 017007 (2006).
- [15] A.V. Balatsky and J.-X. Zhu, *Phys. Rev. B* **74**, 094517 (2006).
- [16] E. Abrahams and C. M. Varma, *Proc. Natl. Acad. Sci.* **97**, 5714 (2000).
- [17] T. Dahm, L.-Y. Zhu, P.J. Hirschfeld, and D. J. Scalapino, *Phys. Rev. B* **71**, 212501 (2005).
- [18] L. Zhu, P.J. Hirschfeld, and D.J. Scalapino, *Phys. Rev. B* **70**, 214503 (2004).
- [19] T. Dahm, P.J. Hirschfeld, D. J. Scalapino, and L.-Y. Zhu, *Phys. Rev. B* **72**, 214512 (2005).
- [20] B.M. Andersen, A. Melikyan, T.S. Nunner, and P.J. Hirschfeld, *Phys. Rev. Lett.* **96**, 097004 (2006).
- [21] T.S. Nunner, W. Chen, B.M. Andersen, A. Melikyan and P.J. Hirschfeld, *Phys. Rev. B* **73**, 104511 (2006).
- [22] M. M. Maska, Z.Sledz, K. Czajka, and M. Mierzejewski, *Phys. Rev. Lett.* **99**, 147006 (2007).
- [23] S. H. Pan *et al.*, *Nature* **413**, 282 (2001).
- [24] K.M. Lang *et al.*, *Nature* **415**, 412 (2002).
- [25] C. Howald, P. Fournier, and A. Kapitulnik, *Phys. Rev. B* **64**, 100504(R) (2001).
- [26] M.H. Hettler and P.J. Hirschfeld, *Phys. Rev. B* **59**, 9606 (1999).
- [27] A. Shnirman, I. Adagideli, P. Goldbart, and A. Yazdani, *Phys. Rev. B* **60**, 7517 (1999).
- [28] S.M. Quinlan, D.J. Scalapino, and N. Bulut, *Phys. Rev. B* **49**, 1470 (1994).
- [29] S.M. Quinlan, P.J. Hirschfeld, and D.J. Scalapino, *Phys. Rev. B* **53**, 8575 (1996).
- [30] M.L. Titov, A.G. Yashenkin, and D.N. Aristov, *Phys. Rev. B* **52**, 10626 (1995).
- [31] J. Paaske and D. Khveshchenko, *Physica C* 341-348 (2000) 265-266.
- [32] D. Duffy, P.J. Hirschfeld, and D.J. Scalapino, *Phys. Rev. B* **64**, 224522 (2001).
- [33] N. Bulut and D.J. Scalapino, *Phys. Rev. B* **53**, 5149 (1996).
- [34] M. Eschrig, *Adv. Phys.* **55**, 47 (2006).
- [35] M.R. Norman, *Phys. Rev. B* **75**, 184514 (2007).
- [36] A. Abanov and A. Chubukov, *Phys. Rev. Lett.* **83**, 1652 (1999).
- [37] A. Abanov, A.V. Chubukov, M. Eschrig, M. R. Norman, and J. Schmalian, *Phys. Rev. Lett.* **89**, 177002 (2002).
- [38] M. Eschrig and M.R. Norman, *Phys. Rev. Lett.* **85**, 3261 (2000).
- [39] J. Fink, A. Koitzsch, J. Geck, V. Zabolotnyy, M. Knupfer, B. Buchner, A. Chubukov, and H. Berger, *Phys. Rev. B* **74**, 165102 (2006).
- [40] I. Eremin, D. K. Morr, A. V. Chubukov, K. H. Bennemann, and M. R. Norman *Phys. Rev. Lett.* **94**, 147001 (2005).
- [41] S. Pailhes *et al.*, *Phys. Rev. Lett.* **93**, 167001 (2004); S. M. Hayden *et al.*, *Nature (London)* **429**, 531 (2004).
- [42] B. Fauqué, Y. Sidis, L. Capogna, A. Ivanov, K. Hradil, C. Ulrich, A.I. Rykov, B. Keimer, and P. Bourges, arXiv:cond-mat/0701052.
- [43] B. W. Hoogenboom, C. Berthod, M. Peter, Ø. Fischer and A. A. Kordyuk, *Phys. Rev. B* **67**, 224502 (2003).
- [44] G.L. de Castro, C. Berthod, A. Piriou, E. Giannini, and Ø. Fischer, arXiv:cond-mat/0703131v2.
- [45] C.M. Varma, P.B. Littlewood, S. Schmitt-Rink, E. Abrahams and A. E. Ruckenstein, *Phys. Rev. Lett.* **63**, 1996 (1989).
- [46] Rajdeep Sensarma, Mohit Randeria, Nandini Trivedi, *Phys. Rev. Lett.* **98**, 027004 (2007).
- [47] A. Kanigel, U. Chatterjee, M. Randeria, M. R. Norman, S. Souma, M. Shi, Z. Z. Li, H. Raffy, and J. C. Campuzano, *Phys. Rev. Lett.* **99**, 157001 (2007).
- [48] J.E. Hoffman, K. McElroy, D.-H. Lee, K. M Lang, H. Eisaki, S. Uchida and J.C. Davis, *Science* **297**, 1148 (2002).
- [49] K. McElroy, D.-H. Lee, J. E. Hoffman, K. M. Lang, J. Lee, E. W. Hudson, H. Eisaki, S. Uchida, and J. C. Davis, *Phys. Rev. Lett.* **94**, 197005 (2005).
- [50] Y. Kohsaka *et al* Submitted (to Nature).
- [51] Lingyin Zhu, W.A. Atkinson, and P. J. Hirschfeld, *Phys. Rev. B* **69**, 060503 (2004).

VIII. APPENDIX 1: MODEL CALCULATION OF SCATTERING BY PAIRING DISORDER

The potential which one adds to the Hamiltonian is then (see Shnirman *et al* PRB 60, 7517 (1999)).

$$\hat{V}_1 = \sum_{\mathbf{k}\mathbf{k}'} (V_{\mathbf{k}} + V_{\mathbf{k}'}) \tau_1, \quad (36)$$

where $V_{\mathbf{k}} = \delta\Delta\phi_{\mathbf{k}}$, and $\phi_{\mathbf{k}}$ is $(\cos k_x - \cos k_y)/2$, such that the average order parameter is $\Delta_0\phi_{\mathbf{k}}$. The parameter $\delta\Delta$ has dimensions of energy and is roughly the amplitude of the off-diagonal modulation. The disorder averaged self-energies then become (with label “ Δ ” for order parameter modulation scattering),

$$\underline{\Sigma}^{\Delta}(\mathbf{k}, \omega) = n_i \sum_{\mathbf{k}'} |V_{\mathbf{k}} + V_{\mathbf{k}'}|^2 \tau_1 \underline{G}(\mathbf{k}', \omega) \tau_1 \quad (37)$$

$$\Sigma_0^{\Delta}(\mathbf{k}, \omega) = n_i (\delta\Delta)^2 \sum_{\mathbf{k}'} \frac{\omega(\phi_{\mathbf{k}}^2 + \phi_{\mathbf{k}'}^2)}{\omega^2 - E_{\mathbf{k}'}^2} \quad (38)$$

$$\Sigma_1^{\Delta}(\mathbf{k}, \omega) = 2n_i (\delta\Delta)^2 \phi_{\mathbf{k}} \sum_{\mathbf{k}'} \frac{\phi_{\mathbf{k}'} \Delta_{\mathbf{k}'}}{\omega^2 - E_{\mathbf{k}'}^2} \quad (39)$$

$$\Sigma_3^{\Delta}(\mathbf{k}, \omega) = -n_i (\delta\Delta)^2 \sum_{\mathbf{k}'} \frac{\xi_{\mathbf{k}'}(\phi_{\mathbf{k}}^2 + \phi_{\mathbf{k}'}^2)}{\omega^2 - E_{\mathbf{k}'}^2} \quad (40)$$

To gain some insight into the energy and momentum dependence of these quantities, we consider a model with a circular Fermi surface and approximate the d -wave order parameter $\Delta_{\mathbf{k}} \simeq \Delta_{\phi} = \Delta_0 \cos 2\phi$. This approximation will not affect the qualitative low-energy dependence of

the scattering rate. As before, we examine the pole of the Green’s function to define the approximate total quasiparticle scattering rate for a quasiparticle on the Fermi surface $\xi_{\mathbf{k}} = 0$ as

$$\Gamma_{el}^{\Delta}(\varphi, \omega) = -\text{Im}\Sigma_0(\varphi, \omega) - \frac{\Delta_{\varphi}}{\omega} \text{Im}\Sigma_1(\varphi, \omega)$$

and estimate the $\omega \ll \Delta_0$ self-energies at the node ($\mathbf{k} = \mathbf{k}_N, \phi = \pi/4$) and antinode ($\mathbf{k} = \mathbf{k}_A, \phi = 0$):

$$\Gamma_{el,N}^{\Delta}(\omega) \approx \frac{1}{4} \Gamma^{\Delta} \frac{\omega^3}{\Delta_0^3} \quad (41)$$

$$\Gamma_{el,A}^{\Delta}(\omega) \approx \frac{5}{4} \Gamma^{\Delta} \frac{\omega}{\Delta_0}, \quad (42)$$

and we have defined $\Gamma^{\Delta} = \pi n_i N_0 (\delta\Delta)^2$. It is clear that, as intuitively expected, the scattering of quasiparticles by order parameter modulations is largest near the antinodes, where the mean order parameter is largest. It is noteworthy that this source of scattering is the only one considered here which gives an anisotropic in \mathbf{k} contribution on the Fermi surface as $\omega \rightarrow 0$ which is largest at the antinode.

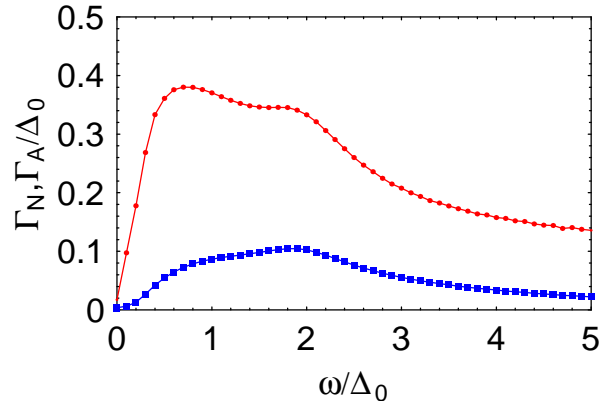


FIG. 15: Off-diagonal scattering rate at node (squares) and antinode (circles) as function of energy ω for toy model where order parameter modulation is confined to bonds neighboring impurity site.